Journal of Casting & Materials Engineering Vol. 10 No. 2 (2026) 34–41
https://doi.org/10.7494/jcme.2026.10.2.34

Microstructure-Erosion Resistance Correlation in High Chromium Cast Iron: A Digital Image Processing Approach

Ottavia Vezzani[a], Annalisa Fortini[a]*, Michele Gragnanini[a], Alessio Suman[a], Nicola Zanini[a]

[a] University of Ferrara, Department of Engineering, Via Saragat 1, 44122 Ferrara, Italy
**e-mail: annalisa.fortini@unife.it*

Received: 20 April 2026/Accepted: 1 June 2026/Published online: 18 June 2026
This article is published with open access at AGH University of Krakow Journals.

Abstract

High chromium cast irons (HCCIs) are widely employed as wear-resistant hardfacing materials in industrial applications where solid particle erosion (SPE) represents a primary degradation mechanism, such as in energy production, mining, and cement manufacturing. The erosive wear resistance of these alloys is strongly dependent on the microstructural features of the primary M_7C_3 carbides, particularly their size, morphology, and spatial distribution within the metallic matrix. The quantitative relationship between carbide distribution homogeneity and erosion resistance has received limited attention in the literature. This study investigates the erosive wear resistance of a Fe-Cr-C cast iron hardfacing alloy and proposes three digital image processing methods to quantitatively characterise the carbide microstructure and correlate it with experimental erosion test results. Optical microscopy combined with image binarisation was used to segment primary M_7C_3 carbides. Three methods were adopted: carbide volume fraction (CVF), minimum inter-carbide distances, and a moving scanning area approach. Erosion tests were conducted according to ASTM G76 guidelines using two Arizona road dust powder grades with two mean diameters under equal kinetic energy conditions. Results show that the erosion rate decreases significantly with the increasing erodent particle size and that carbide distribution homogeneity plays a critical role in determining the erosion resistance. The moving scanning area method proved particularly effective at correlating microstructural coverage with experimental erosion rates.

Keywords:
chromium-rich carbides, hardfacing, image analysis, solid particle erosion, microstructural characterisation

1. INTRODUCTION

Extending the service life of mechanical components operating under severe surface degradation conditions is a major challenge across several industrial sectors, including energy production, mining, and bulk material handling. In applications where components are exposed to the impact of solid particles carried by a fluid stream, erosive wear is a primary failure mechanism, leading to progressive material removal and component replacement costs [1]. A widely adopted strategy to mitigate this problem is the application of hardfacing coatings deposited by welding onto critical surfaces, combining low process cost with the flexibility to treat localised areas and repair damaged zones without replacing entire components [1, 2].

Among hardfacing materials, high chromium cast irons (HCCIs) of the Fe-Cr-C family represent a well-established class of materials due to their hardness, wear and corrosion resistance, properties that are retained even at elevated temperatures [3, 4]. Their chemical composition typically ranges from 2 to 7 wt.% C and from 5 to 36 wt.% Cr and their microstructure consist of primary and eutectic carbides, predominantly of the M_7C_3 type (M = Cr, Fe), embedded in an austenitic, bainitic, or martensitic matrix [5]. The primary M_7C_3 carbides exhibit Vickers hardness values of 1300–1800 HV and serve as the primary barrier against wear, while the metallic matrix provides toughness and load-bearing support to the carbide network [6].

The morphology, size, and spatial distribution of carbides are recognised as critical factors governing the wear resistance of HCCIs [6, 7]. Primary M_7C_3 carbides can exhibit elongated or globular morphologies depending on the solidification conditions and alloy composition [8]. Elongated carbides tend to improve abrasive wear resistance, whereas globular carbides are generally associated with better impact resistance [9]. The carbide volume fraction (CVF), defined as the ratio of the area occupied by carbides to the total analysed area, is the parameter most used in the literature to characterise HCCIs and estimate their wear resistance [10]. Higher CVF values are generally associated with increased hardness and wear resistance, although an excessive CVF can reduce toughness if the matrix is not adequately balanced. CVF can be modified through compositional adjustments, for instance, increasing the Cr content promotes the formation of M_7C_3 and $M_{23}C_6$ carbides, or through destabilisation heat treatments that influence secondary carbide precipitation and matrix hardness [11–13].

The erosive wear behaviour of metallic substrates under solid particle impact depends on multiple factors, including the particle velocity, shape, size, impact angle, and chemical composition of the erodent, as well as the substrate microstructure [14, 15]. Although the erosion resistance of HCCIs has been widely investigated experimentally and numerically [16], the quantitative relationship between microstructural parameters and erosion resistance remains insufficiently explored [7, 10, 17]. In particular, the spatial homogeneity of the carbide distribution, which determines the local probability of matrix exposure to erodent impact, has rarely been addressed through systematic image analysis approaches.

The present study aims to fill this gap by developing and comparing three digital image processing methods for the quantitative characterisation of primary M_7C_3 carbides in a Fe-Cr-C HCCI hardfacing alloy. The methods are correlated with experimental solid particle erosion test results obtained using two erodent powder grades selected based on microstructural inter-carbide distance analysis, in accordance with ASTM G76 guidelines. The results demonstrate that carbide distribution homogeneity, rather than CVF alone, is a key parameter controlling the erosion resistance under the tested conditions.

2. MATERIALS AND METHODS

2.1. Material and sample preparation

The material investigated in this study is a commercial Fe-Cr-C cast iron deposited by hardfacing welding onto a low-carbon steel substrate. The chemical composition of the alloy, determined by Glow Discharge Optical Emission Spectroscopy (GDOES, Spectruma Analytik GDS 650, Hof, Germany), is reported in Table 1. The alloy is hypereutectic, with a primary M_7C_3 carbide fraction solidifying before the eutectic reaction.

Samples with dimensions of 20 mm × 20 mm × 10 mm were prepared in accordance with the requirements of the erosion test bench described in Section 2.2. All samples analysed in this study were extracted from the same hardfacing deposit batch to ensure consistency of welding parameters and microstructural homogeneity across the experimental campaign. Prior to microstructural analysis, sample surfaces were chemically etched using Kalling's reagent (5 g $CuCl_2$, 100 ml HCl, 100 ml C_2H_5OH) for 5 seconds to reveal the structural constituents. Metallographic analysis was performed using a Leica DMi8 A optical metallographic microscope (Leica, Wetzlar, Germany).

2.2. Erosion tests

Solid particle erosion tests were conducted using a dedicated test bench designed in accordance with ASTM G76 guidelines [18]. The apparatus provides control of operational parameters, including the air flow rate, erodent powder feed rate, impact angle, and test duration. A detailed description of the test bench design and its validation is reported in previous works by the authors [19–21].

An impact angle of 15° was selected to simulate the most severe and operationally representative damage conditions for the hardfacing coating under investigation [21]. The erodent material used in all tests was Arizona road dust (ARD), a standardised commercial powder compliant with ISO 12103-1:2016, composed of SiO_2 (75%), Al_2O_3 (20%) and minor oxides (Mg, Fe, and others) [22]. This powder is widely employed in filtration system testing and machine degradation studies. Two powder grades were selected for the erosion tests: ARD Ultrafine (ARD UF) and ARD Medium (ARD M), with mean particle diameters of 4.8 μm and 25.5 μm, respectively. Scanning electron microscopy (SEM) images are shown in Figure 1.

The two powder grades were selected based on the results of the inter-carbide distance analysis described in Section 2.3, to investigate two distinct interaction regimes between erodent particles and substrate microstructure: (i) mean particle diameter smaller than the inter-carbide distance, and (ii) mean particle diameter larger than the inter-carbide distance.

Operational parameters, i.e. air flow rate, powder feed rate and test duration, were determined through computational fluid dynamics (CFD) simulations, maintaining equal kinetic energy conditions for the erodent particles across both test configurations [21]. The powder feed rate was set to 10 g/min. The erosion resistance was quantified through sample mass loss, measured using a Kern ABT 100-5NM precision analytical balance (Kern, Balingen, Germany) with a resolution of 0.01 mg. The erosion rate (ER) was calculated as the ratio between the mass lost by the eroded sample (μg) and the mass of the injected erodent (g), as expressed in Equation (1):

$$ER = \Delta m\_sample / m\_erodent \tag{1}$$

where: Δm_sample is the mass loss of the sample (μg), and m_erodent is the total mass of the erodent injected (g). Ten samples were tested for each condition to ensure the statistical reliability of the results.

Table 1
Chemical composition of the investigated Fe-Cr-C cast iron (wt.%, Fe balance)

C	Mn	Si	Cr	Mo	Nb	W	V	Fe
4.15	0.56	1.08	21.04	2.78	4.09	0.86	0.69	Bal.

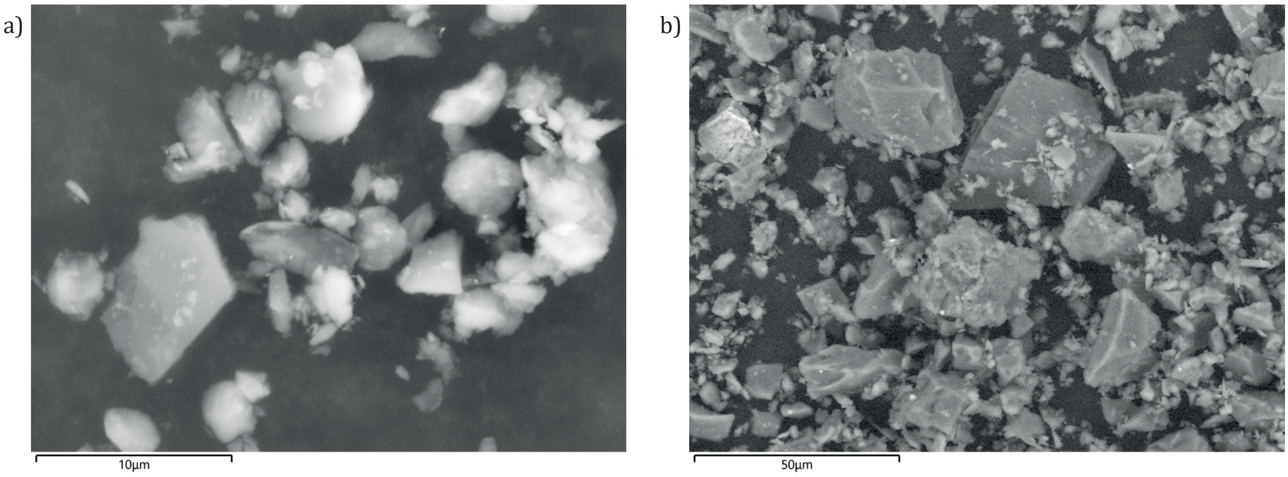

Fig. 1. SEM micrographs of the erodent powders used in the erosion tests: a) ARD UF (d_mean = 4.8 μm); b) ARD M (d_mean = 25.5 μm)

2.3. Microstructural analysis and image processing

Microstructural characterisation was performed on $n = 10$ samples, with $n = 6$ regions of interest (ROIs) identified on each sample, for a total analysed area of 9 mm^2 per sample. Micrographs were acquired at 200× magnification. The microstructure of the investigated alloy consists of polygonal primary M_7C_3 carbides surrounded by a predominantly austenitic matrix with traces of martensite and eutectic carbides. The alloy can therefore be regarded as a two-phase material with a composite-like structure in which the matrix provides toughness and the hard carbides act as reinforcement against wear.

Image processing was performed starting from optical micrographs, which were converted to binary black-and-white images by applying a grey-level threshold using the open-source software ImageJ (Version 1.53e, National Institutes of Health, USA) [23], as shown in Figure 2.

The chromatic contrast between carbides (bright) and matrix (dark) was exploited to segment the carbide phase. The binary images obtained served as the common input for the three analysis methods described as follows.

Method 1: carbide volume fraction (CVF). The carbide volume fraction is defined as the ratio of the total carbide area to the total analysed area, as expressed in Equation (2):

$$CVF = \Sigma\ A\_carbides\ /\ A\_total \quad (2)$$

where: A_carbides is the sum of the areas of all segmented carbide particles, and A_total is the total area of the analysed region. CVF was computed for each ROI across all samples using ImageJ, providing a mean value and associated variability for each region. This parameter represents the most widely used descriptor of HCCI microstructure in the wear literature [10] and serves as the baseline reference method in this study.

Method 2: Minimum inter-carbide distances via Delaunay triangulation. This method was developed to characterise the spatial distribution of primary carbides by computing the minimum edge-to-edge distances between adjacent carbides. Starting from the binary images (Fig. 3a), the centroid coordinates of each carbide particle were extracted after an image cleaning step to remove artifacts and eutectic carbides below a minimum size threshold, to reduce the computational load and focus the analysis on primary carbides (Fig. 3b). Carbide adjacency was determined through Delaunay triangulation applied to the centroid coordinates, and the validity of each triangulation link was verified geometrically to exclude connections crossing other carbide bodies (Fig. 3c).

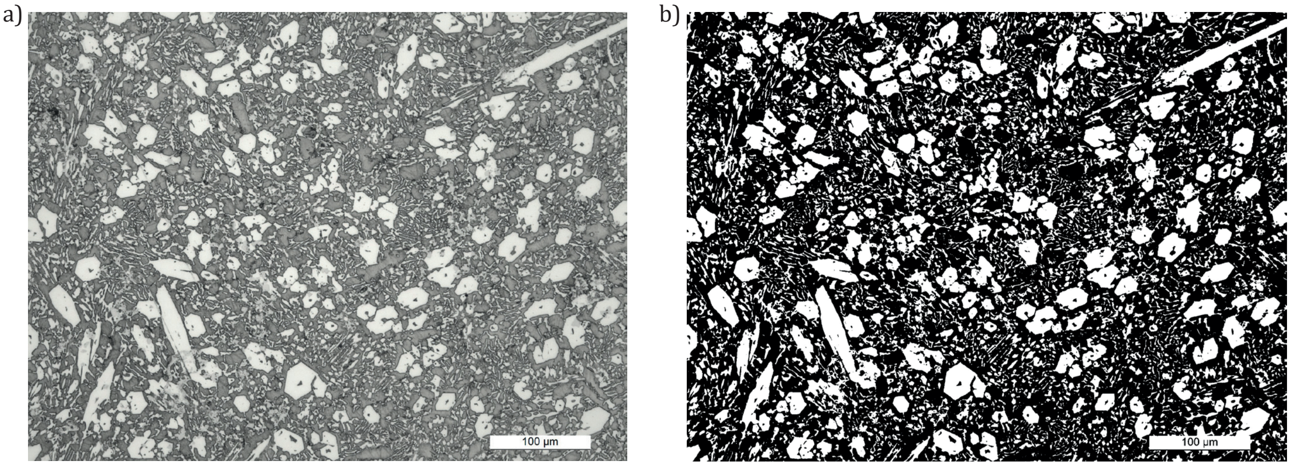

Fig. 2. Example of an optical micrograph of the material under examination: a) original image; b) post-processed binary version

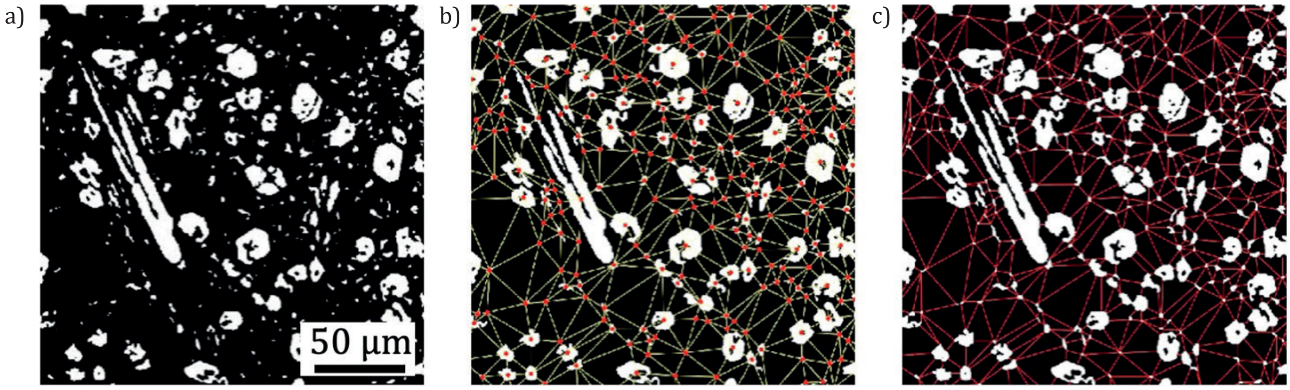

Fig. 3. Image processing steps for Method 2: a) binary image after cleaning; b) carbide centroid coordinates and Delaunay triangulation network with validity check of connections; c) final map of minimum edge-to-edge distances between adjacent carbides

For each valid pair of adjacent carbides, the minimum edge-to-edge distance was then computed as the shortest distance between the respective perimeters, using a dedicated Python script. The resulting distance distributions were represented as boxplot diagrams for each ROI, enabling direct comparison of inter-carbide spacing variability across different microstructural zones. This method provides information exclusively on the spatial homogeneity of the carbide distribution, independently of the carbide area fraction.

Method 3: Moving scanning area. This method was designed to simulate the impact of erodent particles on the substrate microstructure and to quantitatively assess the local carbide coverage experienced by an impacting particle. Starting from the binary images, a square sampling area with a side length equal to the mean equivalent diameter of the erodent powder was defined. The conversion from pixels to micrometres was performed based on the micrograph scale bar using ImageJ. The sampling area was systematically translated across the entire image by centring it on each sampling pixel, and for each position, the coverage ratio (Rc) was computed as the ratio of white pixels (carbides) to total pixels within the sampling area, as expressed in Equation (3):

$$Rc = \mathrm{N\_white} / \mathrm{N\_total} \tag{3}$$

where: N_white is the number of carbide pixels, and N_total is the total number of pixels in the sampling area. To manage the computational cost, a scanning step greater than 1 pixel can be adopted, meaning that the sampling pixel is shifted by a fixed number of pixels in both the horizontal and vertical directions between consecutive evaluations. Border effects were avoided by excluding sampling positions within half the equivalent diameter of the image edges. The procedure was implemented in a Python script, and the output is a frequency histogram of Rc values, representing the probability distribution with which an impacting particle of a given size would encounter a given local carbide coverage. Unlike Method 1 and Method 2, this approach simultaneously accounts for both the carbide area fraction and spatial distribution homogeneity, and it is inherently sensitive to the size of the impacting particle.

3. RESULTS AND DISCUSSION

3.1. Erosion test results

The erosion test results obtained for the two erodent powder grades are summarised in Table 2. Tests were conducted under equal kinetic energy conditions for the erodent particles, so that differences in erosion rate can be attributed to the interaction between particle size and substrate microstructure rather than to differences in impact energy.

Table 2
Erosion test conditions and results

Mean particle diameter [µm]	Impact velocity [m/s]	Kinetic energy [J]	ER [µg/g]
4.8 (ARD UF)	205	6×10^{-8}	48.1 ± 6.7
25.5 (ARD M)	15.9	2×10^{-7}	7.5 ± 2.2

The ARD UF powder (mean diameter 4.8 µm) produced an ER approximately six times higher than that obtained with ARD M (mean diameter 25.5 µm), despite the two conditions being designed to deliver equal kinetic energy to the substrate. This result clearly demonstrates that particle size plays a dominant role in determining erosion severity, independently of the impact energy. The underlying mechanism is related to the interaction between particle size and substrate microstructure: when the mean particle diameter is smaller than the typical inter-carbide spacing, particles preferentially impact the metallic matrix, which offers significantly lower resistance to erosion than the hard carbide phase. Conversely, when the mean particle diameter is comparable to or larger than the inter-carbide spacing, the probability that an impacting particle encounters a carbide increases substantially, and the carbides act as an effective barrier against material removal. SEM analysis of the eroded surfaces confirms this interpretation. Surfaces eroded by ARD UF show extensive and relatively uniform matrix removal with limited carbide involvement, consistent with a regime in which the matrix is the primary target of erosion. Surfaces eroded by ARD M show a qualitatively different damage pattern, with evidence of carbide-particle interactions and reduced matrix exposure, consistent with a regime in which carbides provide effective shielding of the underlying matrix (Fig. 1).

3.2. Method 1 results – carbide volume fraction

The CVF values computed for each of the six ROIs, averaged across all ten samples, are reported in Figure 4. The mean CVF across all ROIs is approximately 25%, with individual ROI values ranging from approximately 20% to 28%. The variability within each ROI, as shown by the error bars in Figure 2, reflects the inherent microstructural inhomogeneity of the hardfacing deposit, a well-known consequence of the solidification conditions during welding. While CVF provides a useful first-order descriptor of carbide content, it has a fundamental limitation as a predictor of erosion resistance: two microstructures with identical CVF values can exhibit very different spatial distributions of carbides and, consequently, very different local erosion behaviours. A microstructure in which carbides are clustered in certain regions leaves large matrix areas exposed to erodent impact, whereas a microstructure with uniformly distributed carbides of the same total area fraction provides more consistent protection. This limitation motivates the development of the complementary methods presented in Sections 3.3 and 3.4.

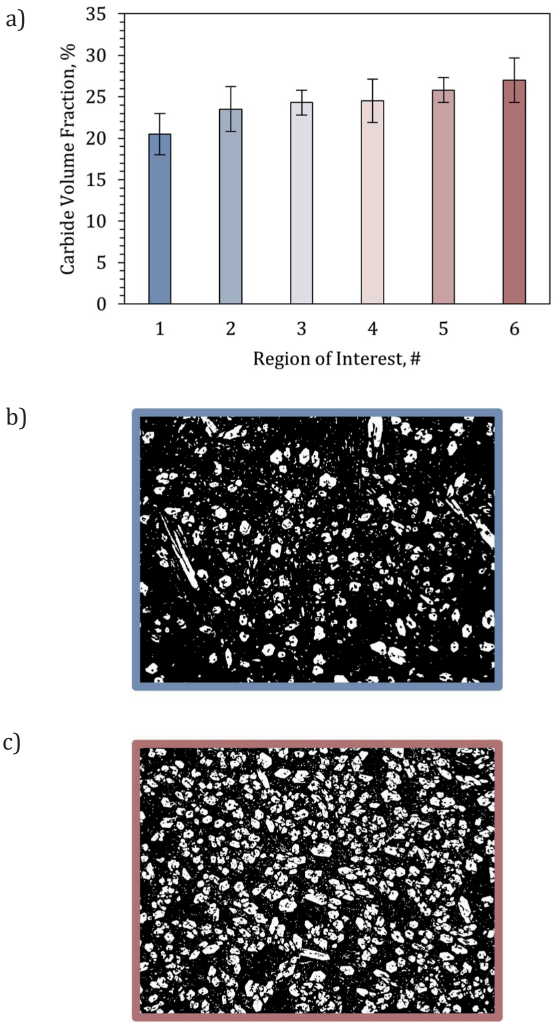

Fig. 4. Carbide volume fraction (CVF) values for each region of interest (ROI), averaged across all ten samples (a); error bars represent the standard deviation; representative optical micrograph of ROI 1, characterised by coarse, elongated primary carbides (a); representative optical micrograph of ROI 6, characterised by finer and more uniformly distributed equiaxed primary carbides (b)

3.3. Method 2 results – minimum inter-carbide distances

The distributions of minimum edge-to-edge distances between adjacent carbides, computed via Delaunay triangulation, are shown as boxplot diagrams for each ROI in Figure 5.

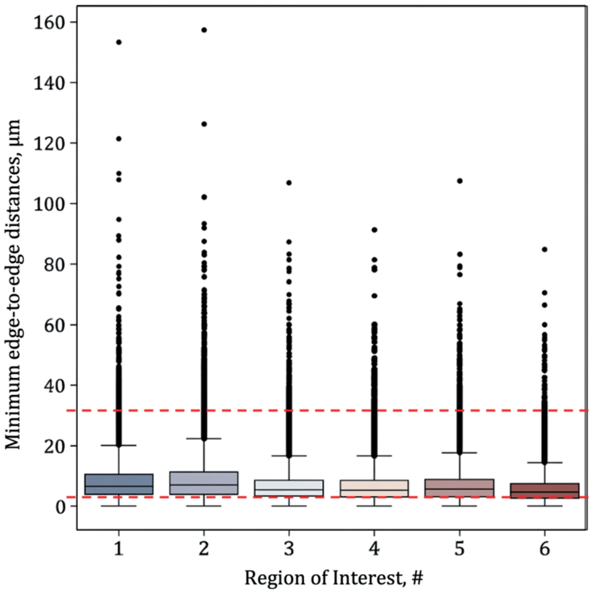

Fig. 5. Boxplot diagrams of minimum edge-to-edge distances between adjacent carbides for each region of interest (ROI). Dashed red lines indicate the mean diameters of the two erodent powders: ARD UF (d_mean = 4.8 µm) and ARD M (d_mean = 25.5 µm)

The distributions are consistently right-skewed across all ROIs, with median values below 10 µm and first quartile values close to or below 5 µm, while the third quartile remains below 25 µm in all cases. Outlier distances exceeding 60–160 µm are present in all ROIs, reflecting the occasional occurrence of large carbide-free matrix zones. The two erodent particle sizes selected for the erosion tests, 4.8 µm and 25.5 µm, are indicated as reference lines in Figure 5. Their relationship with the inter-carbide distance distributions provides a physical interpretation of the erosion results: the mean diameter of ARD UF (4.8 µm) falls below the first quartile of the distance distribution in all ROIs, meaning that the majority of inter-carbide gaps are wider than the impacting particles. Under these conditions, particles can penetrate between carbides and impact the matrix directly, resulting in high erosion rates. The mean diameter of ARD M (25.5 µm) falls near or above the third quartile in most ROIs, meaning that most inter-carbide gaps are narrower than the impacting particles, which therefore interact predominantly with the carbide phase and experience significantly lower erosion. Comparison of ROIs 1 and 2 with ROIs 3 through 6 reveals a higher dispersion of inter-carbide distances in the former, associated with the presence of coarse, elongated carbides interspersed with large carbide-free matrix regions. ROIs 3 through 6, characterised by finer, more equiaxed carbides, exhibit tighter distance distributions with lower median values and fewer extreme outliers. This result demonstrates that Method 2 is sensitive to microstructural inhomogeneity and can identify zones of the deposit that are more vulnerable to erodent penetration between carbides. However, Method 2 presents an intrinsic limitation: it characterises only the spatial distribution of carbides without accounting for their area fraction. Two microstructures with identical inter-carbide distance distributions but different CVF values would be indistinguishable by this method alone. Furthermore, the method does not directly incorporate the geometry of the impacting particle, as it reduces the particle to a point interacting with the inter-carbide space rather than to a finite-area object interacting with a local region of the microstructure. These limitations are addressed by Method 3.

3.4. Method 3 results – moving scanning area

The frequency histograms of the coverage ratio (*Rc*) obtained by the moving scanning area method for ROI 1 and ROI 6, computed using three equivalent particle diameters (5 μm, 10 μm, and 25 μm), are shown in Figure 6. The histograms reveal two qualitatively distinct behaviours depending on the particle size and microstructural zone. For small particle diameters (*Deq* = 5 μm), the *Rc* distributions of both ROIs show a pronounced peak at *Rc* = 0, indicating that a significant fraction of possible impact positions corresponds to areas with no carbide coverage whatsoever. For ROI 1, which is characterised by coarse elongated carbides dispersed in a largely uncovered matrix, this peak reaches approximately 35%, meaning that more than one-third of potential impact positions would result in the particle striking pure matrix. For ROI 6, characterised by finer and more homogeneously distributed equiaxed carbides, the same peak is reduced to approximately 12%, reflecting a substantially lower probability of matrix-only impact. This difference directly explains the high erosion rate observed with ARD UF: under conditions where most particles impact the uncovered matrix, material removal is rapid and severe. As the particle diameter increases to *Deq* = 25 μm, the *Rc* distributions shift markedly. The peak at *Rc* = 0 disappears in both ROIs, and the distributions become centred around the mean CVF value of the analysed area (approximately 12–25% depending on the ROI), reflecting the fact that larger particles necessarily average over a wider area of the microstructure and are therefore less sensitive to local carbide-free zones. This result is consistent with the low erosion rate observed with ARD M: larger particles encounter a mixed carbide-matrix surface regardless of impact position, and the carbides provide effective resistance.

The comparison between ROI 1 and ROI 6 at all particle sizes confirms that Method 3 is sensitive to both the carbide area fraction and spatial distribution homogeneity simultaneously. ROI 6 consistently shows *Rc* distributions shifted towards higher coverage values and with a lower probability of zero-coverage impacts, reflecting its more homogeneous microstructure. This result has a direct practical implication: for a given CVF, a more homogeneous carbide distribution provides better erosion protection, particularly against fine erodent particles. Taken together, the three methods provide a hierarchical and complementary description of the microstructure. Method 1 (CVF) offers a rapid global estimate of the carbide content but cannot distinguish between homogeneous and inhomogeneous distributions. Method 2 characterises the spatial distribution through inter-carbide distances and enables direct identification of critical particle size thresholds, but does not account for the carbide area fraction or particle geometry. Method 3 integrates both coverage and spatial homogeneity into a single particle-size-dependent statistical descriptor, at the cost of higher computational demand. For practical applications, Method 2 is recommended as a rapid screening tool, while Method 3 is recommended for detailed statistical characterisation when the erodent particle size distribution is known.

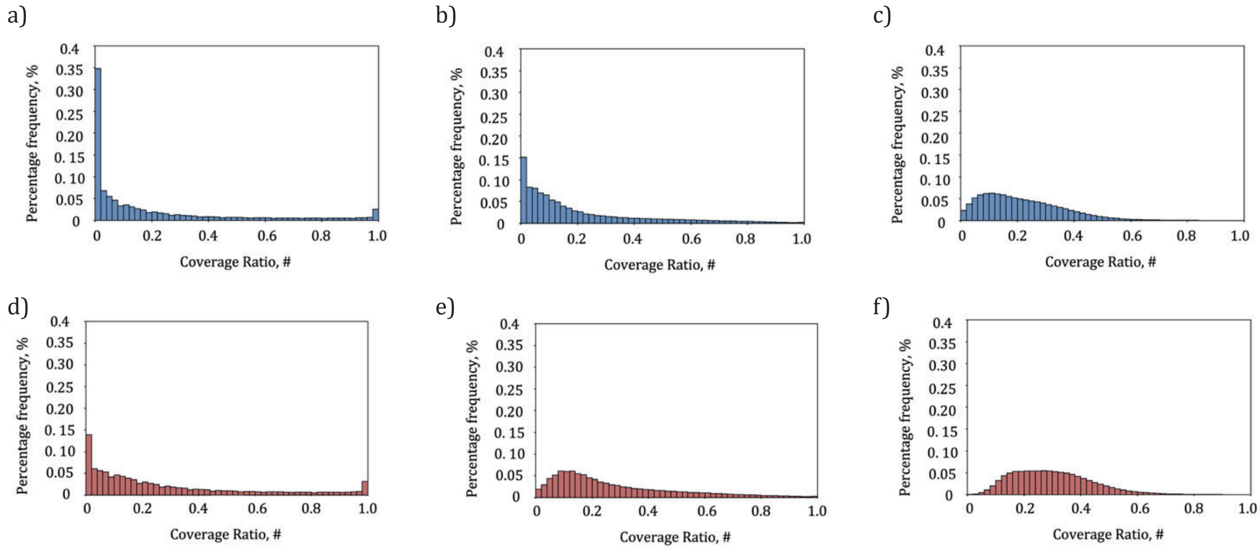

Fig. 6. Percentage frequency histograms of the coverage ratio (*Rc*) obtained by the moving scanning area method for two representative ROIs: a) ROI 1, *Deq* = 5 μm; b) ROI 1, *Deq* = 10 μm; c) ROI 1, *Deq* = 25 μm; d) ROI 6, *Deq* = 5 μm; e) ROI 6, *Deq* = 10 μm; f) ROI 6, *Deq* = 25 μm. ROI 1 is characterised by coarse elongated carbides, ROI 6 by finer and more homogeneously distributed equiaxed carbides

The proposed digital image processing framework is not intrinsically limited to high-chromium cast irons, since it relies on a general microstructural descriptor: the spatial distribution and area coverage of erosion-resistant hard phases within a softer matrix. In principle, the same approach could be extended to other two-phase or particle-reinforced systems, including hypereutectic cast irons, Ni-hard alloys, metal matrix composites, and thermally sprayed coatings, provided that the phases can be segmented reliably. Nevertheless, extrapolation to other systems must be treated with caution.

The predictive relevance of the extracted descriptors depends on whether the controlling erosion mechanisms are governed by the same length-scale relationship between the erodent size, hard-phase spacing, and matrix exposure. Therefore, any extension of the method should include material-specific validation, especially when the morphology, connectivity, toughness, or bonding of the hard phase differs from that of carbides in high-chromium cast irons. In this context, the ratio between the erodent particle size and characteristic microstructural spacing is likely to be a key scaling parameter.

4. CONCLUSIONS

This study investigated the erosive wear resistance of a Fe-Cr-C high chromium cast iron hardfacing alloy through solid particle erosion tests and three digital image processing methods to quantitatively characterise the primary M_7C_3 carbide microstructure. The following conclusions can be drawn:

- The ER decreased significantly with the increasing erodent particle size under equal kinetic energy conditions, with ARD UF (mean diameter 4.8 μm) producing an ER approximately six times higher than ARD M (mean diameter 25.5 μm). This indicates that the ratio of the erodent particle size to the microstructural inter-carbide spacing is a governing parameter of erosion severity, independent of the impact energy.
- The carbide volume fraction (Method 1), while widely used in the literature as a descriptor of HCCI wear resistance, proved insufficient as a standalone predictor of erosion behaviour. It provides no information on the spatial distribution of carbides and cannot distinguish between microstructures with homogeneous and inhomogeneous carbide arrangements that may exhibit substantially different erosion resistances.
- The minimum inter-carbide distance method based on Delaunay triangulation (Method 2) enabled quantitative characterisation of carbide spatial distribution and direct identification of critical erodent particle size thresholds relative to the inter-carbide spacing distribution. ROIs characterised by coarse, elongated carbides showed wider and more dispersed inter-carbide distance distributions, indicating greater vulnerability to fine erodent penetration between carbides. This method is an efficient preliminary screening tool due to its relatively low computational demand.
- The moving scanning area method (Method 3) provided the most complete microstructural descriptor by simultaneously accounting for the carbide area fraction and spatial distribution homogeneity as a function of erodent particle size. The frequency histograms of the coverage ratio showed that microstructural zones with finer, more homogeneously distributed carbides exhibit a significantly lower probability of zero-coverage impacts, particularly for small erodent particles, directly explaining the higher erosion severity observed with ARD UF. This method is recommended for detailed statistical characterisation when the erodent particle size distribution is known, despite its higher computational cost.

The results demonstrate that carbide distribution homogeneity is a critical parameter governing erosion resistance in HCCIs and that its quantitative assessment requires descriptors beyond CVF. The image analysis framework proposed in this study provides a physically grounded statistical tool for correlating microstructure and erosion resistance in hardfacing alloys.

ACKNOWLEDGEMENTS

The authors wish to thank Eng. Andrea Cordone and Eng. Lorenzo Colombani for their support during the experimental erosion tests, and Stephan Gazzini for developing the Python image analysis code.

REFERENCES

[1] Tandon D., Li H., Pan Z., Yu D. & Pang W. (2023). A review on hardfacing, process variables, challenges, and future works. *Metals*, 13(9), 1512. DOI: https://doi.org/10.3390/met13091512.

[2] Badisch E. & Roy M. (2013). Hardfacing for Wear, Erosion and Abrasion. In: M. Roy (Ed.), *Surface Engineering for Enhanced Performance against Wear* (pp. 149–191). Vienna: Springer. DOI: https://doi.org/10.1007/978-3-7091-0101-8.

[3] Budinski K.G. & Budinski S.T. (2021). *Tribomaterials: Properties and Selection for Friction, Wear, and Erosion Applications*. ASM International. DOI: https://doi.org/10.31399/asm.tb.tpsfwea.9781627083232.

[4] Lin C.-M., Chang C.-M., Chen J.-H., Hsieh C.-C. & Wu W. (2009). Microstructural evolution of hypoeutectic, near-eutectic, and hypereutectic high-carbon Cr-based hard-facing alloys. *Metallurgical and Materials Transactions A*, 40, 1031–1038. DOI: https://doi.org/10.1007/s11661-009-9784-6.

[5] Wiengmoon A. (2011). Carbides in high chromium cast irons. *Naresuan University Engineering Journal*, 6(1), 64–71. DOI: https://doi.org/10.14456/nuej.2011.6.

[6] Li P., Yang Y., Shen D., Gong M., Tian C. & Tong W. (2020). Mechanical behavior and microstructure of hypereutectic high chromium cast iron: the combined effects of tungsten, manganese and molybdenum additions. *Journal of Materials Research and Technology*, 9(3), 5735–5748. DOI: https://doi.org/10.1016/j.jmrt.2020.03.098.

[7] Gaqi Y., Kusumoto K., Shimizu K. & Purba R.H. (2023). Effect of carbide orientation on wear characteristics of high-alloy wear-resistant cast irons. *Lubricants*, 11(7), 272. DOI: https://doi.org/10.3390/lubricants11070272.

[8] Liu S., Zhou Y., Xing X., Wang J., Ren X. & Yang Q. (2016). Growth characteristics of primary M7C3 carbide in hypereutectic Fe-Cr-C alloy. *Scientific Reports*, 6, 32941. DOI: https://doi.org/10.1038/srep32941.

[9] Rajicic B.M., Maslarevic A., Bakic G.M., Maksimovic V. & Djukic M.B. (2023). Erosion wear behavior of high chromium cast irons. *Transactions of the Indian Institute of Metals*, 76, 1427–1437. DOI: https://doi.org/10.1007/s12666-022-02860-7.

[10] Sapate S.G. & Rama Rao A.V. (2004). Effect of carbide volume fraction on erosive wear behaviour of hardfacing cast irons. *Wear*, 256(7–8), 774–786. DOI: https://doi.org/10.1016/S0043-1648(03)00527-1.

[11] Karantzalis A.E., Lekatou A. & Diavati E. (2009). Effect of destabilization heat treatments on the microstructure of high-chromium cast iron: A microscopy examination approach. *Journal of Materials Engineering and Performance*, 18, 1078–1085. DOI: https://doi.org/10.1007/s11665-009-9353-6.

[12] Jindal C., Singh Sidhu B., Kumar P. & Singh Sidhu H. (2022). Performance of hardfaced/heat treated materials under solid particle erosion: A systematic literature review. *Materials Today: Proceedings*, 50, 629–639. DOI: https://doi.org/10.1016/j.matpr.2021.03.441.

[13] Kibble K.A. & Pearce J.T.H. (1993). Influence of heat treatment on the microstructure and hardness of 19% high-chromium cast irons. *Cast Metals*, 6(1), 9–15. DOI: https://doi.org/10.1080/09534962.1993.11819121.

[14] Tarodiya R. & Levy A. (2021). Surface erosion due to particle-surface interactions – A review. *Powder Technology*, 387, 527–559. DOI: https://doi.org/10.1016/j.powtec.2021.04.055.

[15] Lindsley B.A. & Marder A.R. (1999). The effect of velocity on the solid particle erosion rate of alloys. *Wear*, 225–229 (Part 1), 510–516. DOI: https://doi.org/10.1016/S0043-1648(99)00085-X.

[16] Oka Y.I. & Yoshida T. (2005). Practical estimation of erosion damage caused by solid particle impact. *Wear*, 259(1–6), 102–109. DOI: https://doi.org/10.1016/j.wear.2005.01.040.

[17] Sapate S.G. & RamaRao A.V. (2006). Erosive wear behaviour of weld hardfacing high chromium cast irons: effect of erodent particles. *Tribology International*, 39(3), 206–212. DOI: https://doi.org/10.1016/j.triboint.2004.10.013.

[18] ASTM International. (2013). ASTM G76-07: Standard Test Method for Conducting Erosion Tests by Solid Particle Impingement Using Gas Jets. ASTM International.

[19] Fortini A., Suman A., Vulpio A., Merlin M. & Pinelli M. (2021). Microstructural and erosive wear characteristics of a high chromium cast iron. *Coatings*, 11(5), 490. DOI: https://doi.org/10.3390/coatings11050490.

[20] Fortini A., Suman A., Zanini N. & Cruciani G. (2022). Erosive wear behavior of high-chromium cast iron: combined effect of erodent powders and destabilization heat treatments. *Coatings*, 12(8), 1218. DOI: https://doi.org/10.3390/coatings12081218.

[21] Fortini A., Suman A. & Zanini N. (2023). An experimental and numerical study of the solid particle erosion damage in an industrial cement large-sized fan. *Engineering Failure Analysis*, 146, 107058. DOI: https://doi.org/10.1016/j.engfailanal.2023.107058.

[22] ISO 12103-1:2016. (2016). Road vehicles – Test contaminants for filter evaluation – Part 1: Arizona test dust. International Organization for Standardization.

[23] Schneider C.A., Rasband W.S. & Eliceiri K.W. (2012). NIH Image to ImageJ: 25 years of image analysis. *Nature Methods*, 9, 671–675. DOI: https://doi.org/10.1038/nmeth.2089.